

Probing tunneling dynamics of dissociative H₂ molecules using two-color bicircularly polarized fieldsZhenning Guo¹,[✉] Yiqi Fang,¹ Peipei Ge,¹ Xiaoyang Yu,¹ Jiguo Wang,¹ Meng Han,^{1,2}
Qihuang Gong,^{1,3,4} and Yunquan Liu^{1,3,4,*}¹*State Key Laboratory for Mesoscopic Physics and Frontiers Science Center for Nano-optoelectronics,
School of Physics, Peking University, Beijing 100871, China*²*Laboratorium für Physikalische Chemie, ETH Zürich, Zürich 8093, Switzerland*³*Collaborative Innovation Center of Quantum Matter, Beijing 100871, China*⁴*Collaborative Innovation Center of Extreme Optics, Shanxi University, Taiyuan, Shanxi 030006, China*

(Received 27 July 2020; revised 24 August 2021; accepted 4 October 2021; published 2 November 2021)

Probing and manipulating the electronic motion in the ultrafast laser molecular interaction provides the pathways for quantum imaging and controlling chemical reactions. Recently, the emerging application of attosecond metrology of ultrafast electron dynamics has accessed the time scale of the most fundamental processes in molecular chemical reactions. Here, we probe the tunneling dynamics of internuclear-dependent dissociative reaction of H₂ with angular streaking using two-color bicircularly polarized femtosecond laser pulses. By measuring high-resolution photoelectron spectroscopy, we disentangle the orientation and internuclear-distance dependent effect of the long-range Coulomb potential and the initial phase on molecular-frame photoelectron momentum distributions, and stereo extract the phase gradient of the tunneling electron wave packets and Wigner time delay during the dissociative ionization using two-color bicircular fields. The work has an insight into the clocking of ultrafast spatiotemporal photoelectron dynamics and the quantum control of molecular chemical processes via sculptured circular fields, which can be applied to polyatomic molecules.

DOI: [10.1103/PhysRevA.104.L051101](https://doi.org/10.1103/PhysRevA.104.L051101)

Imaging and controlling the dynamics of intramolecular electrons and their couplings to nuclear motions in molecular reactions are the main subjects in photoinduced ultrafast chemical and biological processes [1–5]. In the past few decades, the development of femtosecond laser technology has significantly facilitated the studies of intramolecular processes, chemical bond breaking and bond formation, and the interaction of photoactivated molecules with their environment [6–8]. This motivation lies at the heart of femtochemistry [9], a well-established scientific discipline used in most areas of chemical sciences. Recently, the techniques of attosecond light sources operating in the x-ray ultraviolet and x-ray spectral region open the way to directly monitor the electron motion inside molecules [10,11]. Since ultrafast electron dynamics provides the direct access to the “real-time” motion of chemical reactions on the attosecond scale, controlling this electronic motion in the chemical process has been the new paradigm in the emerging field of “attochemistry” [12–14].

The alternative technique to investigate ultrafast electron dynamics of molecular dissociation is attosecond angular streaking (attoclock) with circular femtosecond laser fields [15–20], in which the photoelectron can be streaked into different directions depending on the ionization instant in the molecular frame. Using the attoclock with single-color elliptically polarized pulses, the timing of tunneling ionization for H₂ molecules is shown to be ~ 10 as in Ref. [18].

Alternatively, some recent experimental studies of molecular tunneling ionization show that the molecular orientation will significantly modify the release time of the photoelectron [19,20]. The initial phase structure of the tunneling wave packet in molecules is also shown to have a significant effect on photoelectron momentum distributions [21–24]. The essential element of these phenomena is all about molecular strong-field tunneling processes.

Recently, the geometry of two-color corotating circularly polarized fields has been used as the novel attoclock scheme for atoms [25–28]. Transferring this technique from atoms to molecules would provide an intriguing approach to study the ultrafast laser molecular reaction. In this Letter, we investigate the internuclear-distance and orientation-dependent molecular-frame photoelectron angular distribution and probe tunneling dynamics during the photodissociative reaction (H₂ → H⁺ + H⁰ + e⁻) using the attoclock of bicircular laser fields. The two-color bicircular fields favor the internuclear-distance dependent and time-dependent electron dynamics measurements for dissociative molecules because of the mixed-photon above-threshold dissociation. We have extracted the role of anisotropic long-range Coulomb potential on the electronic wave packet from the measured orientation-dependent photoelectron angular distributions. Then we obtain the initial phase structure of the tunnel-ionized electronic wave packet with respect to the internuclear distance and orientation. We show that the initial phase structure is associated with the Wigner time delay, which carries the electron-migration information from the bound state to the ionization continuum state in the molecular frame.

*yunquan.liu@pku.edu.cn

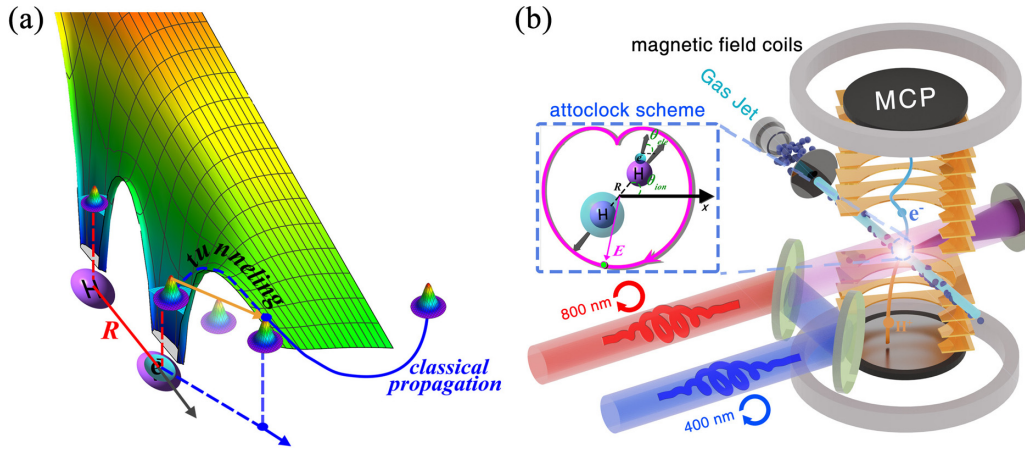


FIG. 1. The attoclock scheme using bicircular fields for the dissociative reaction of H_2 molecules. (a) The combined potential created by the Coulomb field of the H_2 molecule and the laser field. The bound electron escapes the potential through tunneling. (b) The experimental geometry. The fragmentation of H_2 molecules by two-color corotating bicircular fields is measured by the COLTRIMS spectrometer.

In Fig. 1, we show the conceptual overview of experiments. Under the condition of the strong laser field, the Coulomb potential of H_2 molecules is bent and the bound electron wave packet is ionized through tunneling and appears as a classical particle at the tunnel exit, as shown in Fig. 1(a). The electron wave packets releasing from different molecular orientations have different amplitude and initial phase structures. And the stretching of internuclear distance during the dissociative ionization of H_2 molecules leads to the modification of the features of the electronic wave packet. We aim to extract the internuclear-distance dependent initial phase structure in the molecular frame and reconstruct the orientation- and time-resolved electronic dynamics during photodissociation of H_2 molecules.

Experimentally, we employ two-color circularly polarized laser fields to initiate the molecular dissociation. The fundamental field pulse at 800 nm was delivered from an amplified Ti:sapphire laser (0.8 mJ, 25 fs, 3 kHz). The second-harmonic pulse at 400 nm by frequency was produced by frequency doubling with a 250- μm -thick β -barium borate crystal. Then the two-color circularly polarized fields were generated from each arm in a Mach-Zehnder interferometer scheme. The peak intensities of the fundamental field and the second harmonic were calibrated to be $I_{800} = 8.92 \times 10^{13} \text{ W/cm}^2$ and $I_{400} = 2.23 \times 10^{13} \text{ W/cm}^2$. The phase between the two-color fields was finely adjusted by using a pair of fused silica wedges. The synthesized bicircular field can be used to clock the dissociative ionization channels of H_2 ($\text{H}_2 \rightarrow \text{H}^+ + \text{H}^0 + e^-$), as shown in Fig. 1(b). Within the axis recoil approximation, the instantaneous molecular orientation is mostly along the ionic direction at the instance of bond breaking [19]. We then constructed the molecular-frame photoelectron momentum distributions.

The light was then focused by a silver-coated concave mirror ($f = 75 \text{ mm}$) onto a supersonic gas jet of H_2 inside an ultrahigh vacuum chamber of cold-target recoil-ion reaction momentum spectroscopy (COLTRIMS) [Fig. 1(b)] [29]. The supersonic gas jet was created by expanding hydrogen gas at a pressure of 2 bar through a 30- μm diameter nozzle into the vacuum. A homogeneous static electric field

($\sim 4.6 \text{ V/cm}$) and magnetic field ($\sim 6.5 \text{ G}$) were employed to accelerate and guide the ionized ions and electrons to the microchannel plate detectors along the time-of-flight (TOF) axis. Three-dimensional photoelectron momentum distributions were retrieved from position and TOF measurements. For the dissociative ionization of H_2 , we detected the momentum of photoelectrons e^- and H^+ ions coincidentally. The kinetic energy of the neutral H^0 atom (not detectable in the present experiment) was deduced from the momentum conservation of the ejected fragments from the breaking molecule.

The measured electron-nuclear joint energy spectrum of the photoelectron E_e with respect to the nuclear E_N kinetic energies is shown in Fig. 2(a), where E_N is the total kinetic energy of the ejected proton H^+ and the neutral fragment

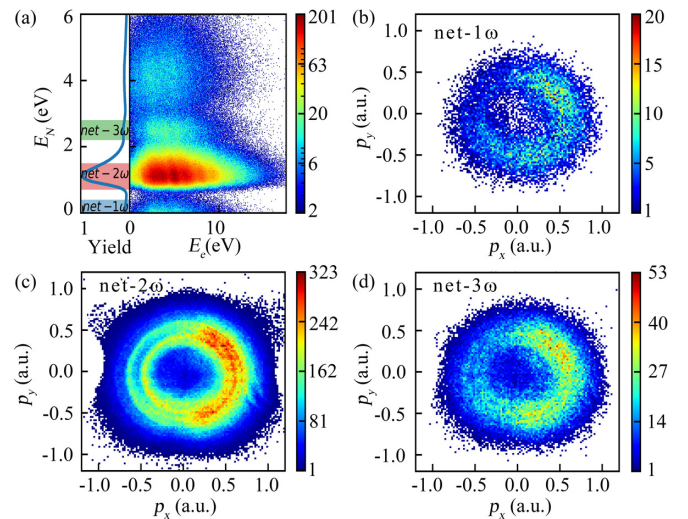


FIG. 2. Measured joint photoelectron-nuclear energy spectrum and two-dimensional photoelectron momentum distributions. (a) The joint photoelectron-nuclear energy spectrum of above-threshold multiphoton dissociative ionization. The nuclear energy spectrum integrated over the electron energy spectrum is shown in the left panel. (b)–(d) Measured photoelectron angular distributions correlated to the 1ω channel (b), 2ω channel (c), and 3ω channel (d).

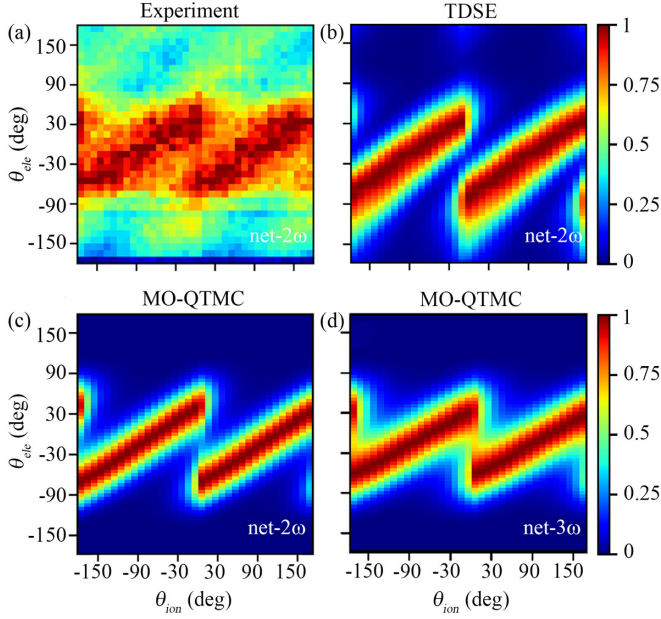


FIG. 3. (a) The measured correlated electron emission angle with the H^+ ion emission angle. (b) The simulated result using the TDSE for the net- 2ω channel. (c), (d) The simulated correlated electron emission angle with H^+ ion emission angle for the net- 2ω and net- 3ω channels using the MO-QTMC model.

H^0 . We illustrate the potential energy curves and dissociation channels of H_2^+ in the two-color bicircular laser fields in Fig. S1 [30]. One can observe that there are three favored dissociative reaction channels for H_2^+ , i.e., the one-photon (net- 1ω) channel (it propagates along the $1s\sigma_g$ state with the one-800 nm-photon transition to the $2p\sigma_u$ state, then dissociating along the $2p\sigma_u$ state), the net-two-photon (net- 2ω) channel (it propagates along the $1s\sigma_g$ state with one-400 nm-photon transition to the $2p\sigma_u$ state, dissociating along the $2p\sigma_u$ state), and the net-three-photon (net- 3ω) channel (it first propagates along the $1s\sigma_g$ state with the three-800nm-photon transition to the $2p\sigma_u$ state, then dissociating along the $2p\sigma_u$ state). For the net- 2ω channel, the ionization-created H_2^+ dissociates at $R = 3.7$ a.u. (atomic unit) and the nuclear kinetic energy release E_N peaks around 1.2 eV. The net- 1ω (bond softening) channel occurs at $R = 4.8$ a.u., resulting in a lower E_N . And for the net- 3ω channel, the internuclear distance R is 2.6 a.u., with a higher E_N at 2.3 eV. In Figs. 2(b)–2(d), we show the measured photoelectron momentum distributions in the polarization plane (laboratory frame), which are measured coincidentally with the net- 1ω , net- 2ω , and net- 3ω dissociative channels, respectively. These distributions generally reveal the feature of the crescent-shaped lobe because the electric field of two-color bicircular fields maximizes only once per 800-nm laser cycle [26,31].

Since there are three involved internuclear-distance reaction channels, we then analyze the internuclear-distance dependent molecular-frame photoelectron emission dynamics. The measured correlation of the electron emission angle (θ_{ele}) and the H^+ ion emission angle (θ_{ion}) for the net- 2ω channel is shown in Fig. 3(a). It is normalized with the maximum yields of photoelectron angular distribution at each H^+

emission angle. The experimental results, corresponding to the net- 1ω and net- 3ω channels, are shown in Figs. S2(a) and S2(d) [30]. The θ_{ele} varies as a function of θ_{ion} and the overall distributions are divided into two tilted strips at $\theta_{ion} = 0$. Note that, the θ_{ion} can be assumed to be the bond direction at the instant of dissociation [15]. Thus, this spectrum reveals the orientation-dependent photoelectron angular distribution.

To analyze the physical origin of orientation-dependent photoelectron angular distribution, we have performed the simulation with the molecular quantum-trajectory Monte Carlo (MO-QTMC) for H_2 molecules [32–34]. In the MO-QTMC model, we analytically obtain the internuclear-dependent amplitude and initial phase structure of the tunnel-ionized electron wave packet of H_2 molecules at the tunnel exit. When the electron wave packet is released at the instantaneous laser field pointing to β , the initial phase ϕ_{ini} and amplitude M_{struc} of the ionized electron wave packet can be written as

$$\begin{aligned} \tan \phi_{ini} &= -\tan \left[\frac{p_i R \sin(\theta_{ion} - \beta)}{2} \right] \tanh \left[\frac{R \cos(\theta_{ion} - \beta)}{2} \right] \\ &\quad \times \sqrt{2I_p + p_i^2}, \\ M_{struc}^2 &= \left\{ \cos \left[\frac{p_i R \sin(\theta_{ion} - \beta)}{2} \right] \cosh \left[\frac{R \cos(\theta_{ion} - \beta)}{2} \right] \right. \\ &\quad \left. \times \sqrt{2I_p + p_i^2} \right\}^2 \\ &\quad + \left\{ \sin \left[\frac{p_i R \sin(\theta_{ion} - \beta)}{2} \right] \sinh \left[\frac{R \cos(\theta_{ion} - \beta)}{2} \right] \right. \\ &\quad \left. \times \sqrt{2I_p + p_i^2} \right\}^2. \end{aligned} \quad (1)$$

Here R and I_p are the internuclear distance and ionization potential, respectively. $\theta_{ion} - \beta$ is the ion emission angle θ_{ion} with respect to the instantaneous laser field direction β . The initial transverse momentum p_i is perpendicular to the instantaneous laser field direction. M_{struc}^2 is the orientation-dependent ionization probability, which mimics the shape of the H_2 molecular orbital and maximizes along the molecular axis. Hence, the tunneling probability is given by $W(t, p_i) = M_{struc}^2 W_0(t, p_i)$, where

$$\begin{aligned} W_0(t, p_i) &= \frac{(2I_p)^{5/2}}{|F(t)|^2 (2I_p + p_i^2)} \left(\frac{2(2I_p)^{3/2}}{|F(t)|} \right)^{2/\sqrt{I_p}} \\ &\quad \times \exp \left(-\frac{2(2I_p)^{3/2}}{3|F(t)|} - \frac{\sqrt{2I_p} p_i^2}{|F(t)|} \right). \end{aligned} \quad (2)$$

Here, $F(t)$ is the instantaneous laser field when the electron is released. After tunneling, the electron's evolution is governed by the Newtonian equations of motion, $\ddot{\mathbf{r}} = -(\mathbf{r} - \mathbf{R}/2)/(2|\mathbf{r} - \mathbf{R}/2|^3) - (\mathbf{r} + \mathbf{R}/2)/(2|\mathbf{r} + \mathbf{R}/2|^3) - \mathbf{F}(t)$. The phase of each quantum trajectory is given by $\phi_{ini} + S$, where ϕ_{ini} is the initial phase given by Eq. (1) and S is the classical action after tunneling, given by $S = -\int_{t_0}^{t_f} [|\mathbf{p}(t)|^2/2 - 1/(2|\mathbf{r} - \mathbf{R}/2|) - 1/(2|\mathbf{r} + \mathbf{R}/2|) + I_p] dt$. Here $\mathbf{p}(t)$ is the electron momentum during the propagation. In the MO-QTMC, the effect of the orientation-dependent

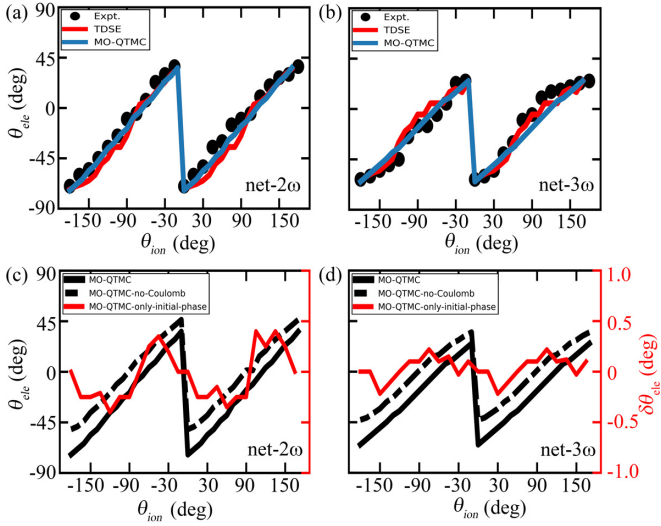


FIG. 4. (a), (b) The most probable electron emission angle θ_{ele} extracted from the experiment, TDSE and MO-QTMC model for the net- 2ω (a) and the net- 3ω (b) channels, respectively. (c), (d) The most probable electron emission angle simulated using the MO-QTMC model for the net- 2ω (c) and net- 3ω (d) channels with and without the long-range Coulomb potential, respectively. The black solid and dashed curves depict the results of MO-QTMC with and without the Coulomb interaction after tunneling, respectively. The red curves indicate the deflect angle because of the initial phase.

ionization probability, the long-range Coulomb potential, the internuclear distance, and the initial phase structure have been included to calculate the photoelectron angular emission distribution in the molecular frame. Figs. 3(c) and 3(d) show the simulations corresponding to the net- 2ω channel ($R = 3.7$ a.u.) and the net- 3ω channel ($R = 2.6$ a.u.), respectively. And the result for the net- 1ω ($R = 4.8$ a.u.) is shown in Fig. S2(c). For the larger internuclear distance, it has a larger electron deflected angle. This indicates the electronic wave packet motion during the dissociative reaction of H_2 molecules.

We have solved the time-dependent Schrödinger equation (TDSE) for strong-field ionization of H_2^+ [30] as the benchmark, as shown in Fig. 3(b). For the net- 1ω and net- 3ω channels, the simulated results of TDSE solutions are shown in Fig. S2 [30]. In Figs. 4(a) and 4(b), we show the most probable electron emission angle as a function of θ_{ion} extracted from the experimental and calculated results using TDSE and MO-QTMC for the net- 2ω and net- 3ω channels. The result for the net- 1ω channel is shown in Fig. S3(a) [30]. The calculated results using both the *ab initio* theory and the MO-QTMC model agree well with the measurements. For the larger internuclear distance, the electron deflected angle is larger.

As seen in the MO-QTMC model, the calculated photoelectron angular distributions include the effect of the orientation-dependent ionization probability, the long-range Coulomb potential, the internuclear distance and the initial phase structure. The emission angle of photoelectrons depends on the molecular orientation mainly from those three factors. In Figs. 4(c) and 4(d), we compare the most prob-

able electron emission angle with respect to the molecular orientation using MO-QTMC with or without the long-range Coulomb interaction (the black solid and dashed curves) for the net- 2ω and net- 3ω channels, respectively. Results corresponding to the net- 1ω channel are given in Fig. S3(b) [30]. Subtracting the deflected angle with and without the long-range Coulomb potential, as seen in Fig. S4 [30], we can find that the molecular Coulomb interaction after tunneling introduces an anisotropic angular offset $\Delta\theta_{\text{ele}}$ for the electron emission angle with respect to the molecular orientation. The long-range Coulomb potential will induce a larger deflected angle when the molecular orientation is parallel with the maximum field direction.

Besides that, the electron deflected angle with respect to the molecular orientation in the bicircular field is the natural consequence of the orientation-dependent ionization probability. The ionization probability is a product of the orientation-dependent probability M_{struc}^2 [Eq. (1)] and the exponential ionization probability W_0 [Eq. (2)] for the H_2 molecule. When the molecular orientation changes, the ionization probability differs due to the effect of M_{struc}^2 . As a result, the release time of the photoelectron will be altered, which yields a relative change of the photoelectron angular distribution. Because the final electron emission angle (θ_{ele}) is mainly determined by the vector potential at the instant of tunneling (i.e., the release time), the photoelectron release-time modification because of molecular orientation can be directly obtained from the deflected angle θ_{ele} . The observed variations of the most-probable photoelectron emission angle θ_{ele} are $\sim 55^\circ$, $\sim 47^\circ$ and $\sim 38^\circ$ for the net- 1ω , net- 2ω , and net- 3ω channels for the 0° orientation. We then can calculate the corresponding time shift ~ 440 attoseconds (as), ~ 376 as and ~ 304 as with respect to the maximum of bicircular fields for those three dissociative channels, respectively. The internuclear distance and molecular orientation have very crucial effects on the release time of the photoelectron and will modify the electron deflected angle with respect to the molecular orientation.

The initial phase ϕ_{ini} of the tunneling wave packet depends on the internuclear distance R and the initial transverse momentum p_i , which will also have a certain effect on the electron deflected angle. In Figs. 4(c) and 4(d), we show the deflected angle $\delta\theta_{\text{ele}}$ because of the initial phase for the net- 2ω and net- 3ω channels, respectively. The results for the net- 1ω channel are illustrated in Fig. S3(b) [30]. The oscillation amplitude of the deflected angle $\delta\theta_{\text{ele}}$ gradually increases with the increasing internuclear distance, which means it will be deflected to a larger angle at a larger internuclear distance.

In Figs. 5(a) and 5(b), we show the calculated initial phase ϕ_{ini} with respect to p_i for different molecular orientation angles, corresponding to the net- 2ω and net- 3ω channels, respectively. Results for the net- 1ω are shown in Fig. S5(a). We can see that the initial phase ϕ_{ini} almost depends linearly on p_i and the slopes vary at different orientation angles. The slope gradually increases with the growing internuclear distance at the same orientation angle. To visual the linear relation, we show the initial phase gradient $\phi'_{\text{ini}} = \partial\phi_{\text{ini}}/\partial p_i$ (i.e., the slope of the initial phase with respect to the initial momentum) as a function of the molecular orientation θ_{ion} in Figs. 5(c) and

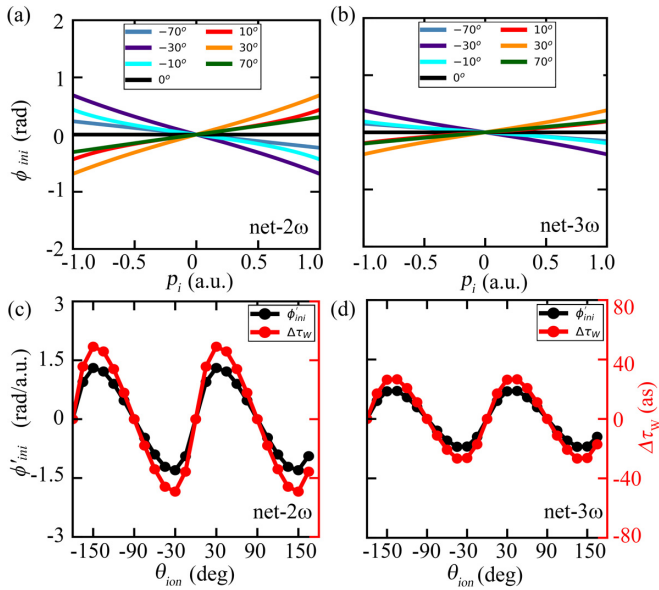


FIG. 5. (a), (b) The initial phase ϕ_{ini} with respect to the initial transverse momentum p_i for the net- 2ω (a) and net- 3ω (b) channels. (c), (d) The initial phase gradient ϕ'_{ini} and the Wigner time delay $\Delta\tau_w$ in the molecular frame for the net- 2ω (c) and net- 3ω (d) channels.

5(d). And the result for the net- 1ω is shown in Fig. S5(b) [30]. One can see the ϕ'_{ini} also oscillates with the orientation angle for different dissociative channels.

As known, the temporal response to the phase shift is defined as the Wigner time delay τ_w [35], which is given by the derivative of the initial phase of the electron wave packet with

respect to the energy, i.e., $\Delta\tau_w = \hbar\partial\phi_{\text{ini}}/\partial E = \hbar m_e \phi'_{\text{ini}}/p$ [24]. Here, $m_e = 1$ a.u. is the electron's mass, the reduced Planck constant $\hbar = 1$ a.u., and p is the final momentum of photoelectrons. Thus, the molecular-frame Wigner time delay $\Delta\tau_w$ (the red curve) is closely related to the initial phase gradient ϕ'_{ini} . We show the molecular-frame Wigner time delay with respect to the orientation angle in Figs. 5(c) and 5(d) on the right vertical scale for the net- 2ω and net- 3ω channels, respectively. The molecular-frame Wigner time delay for the net- 1ω channel is shown in Fig. S5(b) [30]. The differences of the Wigner time $\Delta\tau_w$ in the molecular frame are ± 68 as, ± 48 as and ± 26 as for the net- 1ω , net- 2ω and net- 3ω channels, respectively. The Wigner time delay difference in the molecular frame originates from the initial phase, encoding the electron tunneling dynamics of the dissociative ionization at different internuclear distances.

In summary, we have introduced two-color bicircular fields to probe the tunneling dynamics of dissociative ionization of H_2 . Measuring the internuclear-distance photoelectron momentum spectroscopy in the molecular frame, we have tracked the ultrafast electron dynamics of photodissociation of oriented molecules and disentangled the molecular-frame initial phase structure of the tunneling electronic wave packet at different nuclear distances. Specifically, we have reconstructed the internuclear-distance dependent molecular-frame Wigner time delay. The experimental advances may pave the road towards probing ultrafast electron dynamics of polyatomic molecules using sculptured circular fields.

We are grateful for the support by the National Science Foundation of China (Grants No. 92050201, No. 11774013, and No. 11527901).

-
- [1] T. Bredtmann, D. J. Diestler, Si-Dian Li, J. Manz, J. F. Pérez-Torres, W. Tian, Y. Wu, Y. Yang, and Hua-Jin Zhai, *Phys. Chem. Chem. Phys.* **17**, 29421 (2015).
- [2] P. Baum and F. Krausz, *Chem. Phys. Lett.* **683**, 57 (2017).
- [3] A. Marais, *J. R. Soc. Interface* **15**, 20180640 (2018).
- [4] H. B. Gray and J. R. Winkler, *Q. Rev. Biophys.* **36**, 341 (1999).
- [5] D. M. Villeneuve, P. Hockett, M. J. J. Vrakking, and H. Niikura, *Science* **356**, 1150 (2017).
- [6] T. S. Rose, M. J. Rosker, and A. H. Zewail, *J. Chem. Phys.* **88**, 6672 (1988).
- [7] K. Mizuse, N. Sakamoto, R. Fujimoto, and Y. Ohshima, *Phys. Chem. Chem. Phys.* **22**, 10853 (2020).
- [8] N. E. Hemriksen, *Chem. Phys.* **442**, 2 (2014).
- [9] A. H. Zewail, *J. Phys. Chem. A* **104**, 5660 (2000).
- [10] Z. Chang, P. B. Corkum, and S. R. Leone, *J. Opt. Soc. Am. B* **33**, 1081 (2016).
- [11] T. Gaumnitz, A. Jain, Y. Pertot, Ma. Huppert, I. Jordan, F. Ardana-Lamas, and H. J. Wörner, *Opt. Express* **25**, 27506 (2017).
- [12] M. Nisoli, P. Decleva, F. Calegari, A. Palacios, and F. Martín, *Chem. Rev.* **117**, 10760 (2017).
- [13] F. Lépine, M. Y. Ivanov, and M. J. J. Vrakking, *Nat. Photon.* **8**, 195 (2014).
- [14] S. R. Leone *et al.*, *Nat. Photon.* **8**, 162 (2014).
- [15] A. Staudte, S. Patchkovskii, D. Pavičić, H. Akagi, O. Smirnova, D. Zeidler, M. Meckel, D. M. Villeneuve, R. Dörner, M. Yu. Ivanov, and P. B. Corkum, *Phys. Rev. Lett.* **102**, 033004 (2009).
- [16] H. Akagi, T. Otobe, A. Staudte, A. Shiner, F. Turner, R. Dörner, D. M. Villeneuve, and P. B. Corkum, *Science* **325**, 1364 (2009).
- [17] U. S. Sainadh, R. T. Sang, and I. V. Litvinyuk, *J. Phys. Photon.* **2**, 042002 (2020).
- [18] W. Quan, V. V. Serov, M. Z. Wei, M. Zhao, Y. Zhou, Y. L. Wang, X. Y. Lai, A. S. Kheifets, and X. J. Liu, *Phys. Rev. Lett.* **123**, 223204 (2019).
- [19] A. Khan, D. Trabert, S. Eckart, M. Kunitski, T. Jahnke, and R. Dörner, *Phys. Rev. A* **101**, 023409 (2020).
- [20] J. Yan, W. Xie, M. Li, K. Liu, S. Luo, C. Cao, K. Guo, W. Cao, P. Lan, Q. Zhang, Y. Zhou, and P. Lu, *Phys. Rev. A* **102**, 013117 (2020).
- [21] M. Meckel, A. Staudte, S. Patchkovskii, D. M. Villeneuve, P. B. Corkum, R. Dörner, and M. Spanner, *Nat. Phys.* **10**, 594 (2014).
- [22] M. Han, P. Ge, J. Wang, Z. Guo, Y. Fang, X. Ma, Y. Deng, H. J. Wörner, Q. Gong, and Y. Liu, *Nat. Photon.* **15**, 765 (2021).
- [23] S. Eckart, *Phys. Rev. Res.* **2**, 033248 (2020).

- [24] D. Trabert, S. Brennecke, K. Fehre, N. Anders, A. Geyer, S. Grundmann, M. S. Schöffler, L. Ph. H. Schmidt, T. Jahnke, R. Dörner, M. Kunitski, and S. Eckart, *Nat. Commun.* **12**, 1697 (2021).
- [25] M. Han, P. Ge, Y. Shao, Q. Gong, and Y. Liu, *Phys. Rev. Lett.* **120**, 073202 (2018).
- [26] P. Ge, M. Han, Y. Deng, Q. Gong, and Y. Liu, *Phys. Rev. Lett.* **122**, 013201 (2019).
- [27] N. Eicke and M. Lein, *Phys. Rev. A* **99**, 031402(R) (2019).
- [28] N. Eicke, S. Brennecke, and M. Lein, *Phys. Rev. Lett.* **124**, 043202 (2020).
- [29] J. Ullrich, R. Moshhammer, A. Dorn, R. Dörner, L. Ph. H. Schmidt, and H. Schmidt-Böcking, *Rep. Prog. Phys.* **66**, 1463 (2003).
- [30] See Supplemental Material at <http://link.aps.org/supplemental/10.1103/PhysRevA.104.L051101> for the dissociation channels along the potential surface and the experimental results for the $\text{net-}1\omega$.
- [31] C. A. Mancuso, D. D. Hickstein, P. Grychtol, R. Knut, O. Kfir, X.-M. Tong, F. Dollar, D. Zusin, M. Gopalakrishnan, C. Gentry, E. Turgut, J. L. Ellis, M.-C. Chen, A. Fleischer, O. Cohen, H. C. Kapteyn, and M. M. Murnane, *Phys. Rev. A* **91**, 031402(R) (2015).
- [32] M. M. Liu, M. Li, C. Wu, Q. Gong, A. Staudte, and Y. Liu, *Phys. Rev. Lett.* **116**, 163004 (2016).
- [33] M.-M. Liu and Y. Liu, *J. Phys. B.* **50**, 105602 (2017).
- [34] M. M. Liu, M. Han, P. Ge, C. He, Q. Gong, and Y. Liu, *Phys. Rev. A* **97**, 063416 (2018).
- [35] E. P. Wigner, *Phys. Rev.* **98**, 145 (1955).